

Local electronic structure of interstitial hydrogen in MgH_2 inferred from muon study

Ryosuke Kadono¹, Masatoshi Hiraishi², Hirotaka Okabe³,
Akihiro Koda^{1,4}, and Takashi U Ito⁵

¹ Muon Science Laboratory and Condensed Matter Research Center, Institute of Materials Structure Science, High Energy Accelerator Research Organization (KEK-IMSS), Tsukuba, Ibaraki 305-0801, Japan

² Institute of Quantum Beam Science, Graduate School of Science and Engineering, Ibaraki University, Mito, Ibaraki 310-8512, Japan

³ Institute for Materials Research, Tohoku University, Sendai 980-8577, Japan

⁴ Department of Materials Structure Science, The Graduate University for Advanced Studies (Sokendai), Tsukuba, Ibaraki 305-0801, Japan

⁵ Advanced Science Research Center, Japan Atomic Energy Agency, Tokai, Ibaraki 319-1195, Japan

E-mail: ryosuke.kadono@kek.jp

Abstract. Magnesium hydride has great potential as a solid hydrogen (H) storage material because of its high H storage capacity of 7.6 wt%. However, its slow hydrogenation and dehydrogenation kinetics and the high temperature of 300 °C required for decomposition are major obstacles to small-scale applications such as automobiles. The local electronic structure of interstitial H in MgH_2 is an important fundamental knowledge in solving this problem, which has been studied mainly based on density functional theory (DFT). However, few experimental studies have been performed to assess the results of DFT calculations. We have therefore introduced muon (μ) as pseudo-H into MgH_2 and investigated the corresponding interstitial H states by analyzing their electronic and dynamical properties in detail. As a result, we observed multiple μ states similar to those observed in wide-gap oxides, and found that their electronic states can be attributed to relaxed-excited states associated with donor/acceptor levels predicted by the recently proposed “ambipolarity model”. This provides an indirect support for the DFT calculations on which the model is based via the donor/acceptor levels. An important implication of the muon results for improved hydrogen kinetics is that dehydrogenation, serving as a *reduction* for hydrides, stabilises the interstitial H^- state.

Keywords: hydrogen storage, interstitial hydrogen, electronic structure, muon spin rotation

1. Introduction

Hydrogen (H) storage materials are attracting attention for their importance as a core energy carrier in hydrogen energy production and utilization systems toward a decarbonized society [1, 2]. Therefore, there is a need for materials that can safely and efficiently store H and easily control the absorption and release of H. In particular, solid materials such as metal hydrides are characterized by high safety and high volume and weight densities, and there are great expectations for their practical use [3].

Among metal hydrides, magnesium hydrides have always attracted considerable interest. Magnesium reacts reversibly with H to form hydride (MgH_2), which has great potential as a solid H storage material because of its high H storage capacity of 7.6 wt%. However, its slow hydrogenation and dehydrogenation rates and the high temperature of 300 °C required for decomposition are major obstacles to small-scale applications such as automobiles [3, 4]. Several experimental and theoretical studies have already been published on H kinetics in MgH_2 to solve the problem. However, most of them have concentrated only on macroscopic analysis by thermodynamic measurements of the effects of ball milling, heavy ion irradiation, or the addition of trace metals or their oxides on the reaction kinetics [5, 6, 7, 8, 9, 10, 11].

Understanding the atomic-level mechanisms of hydrogenation and dehydrogenation processes is key to engineering solutions for accelerating these processes and lowering the decomposition temperatures. In MgH_2 , the local electronic state of isolated H at the interstitial site (H_i) is also one of the most fundamental pieces of information in elucidating the rate-limiting processes in H kinetics. Meanwhile, experimental means to study the microscopic states of isolated H in trace amounts in solids are limited, and so far the *ab initio* calculations based on density functional theory (DFT) have been the primary tool for this purpose [10, 12, 13]. However, there have been few experimental studies to assess the theoretical predictions to date.

To overcome this situation, we have introduced positive muon (μ^+) into MgH_2 , and investigated their electronic states and dynamical properties in detail using muon spin rotation (μ SR). Because the mass of μ^+ is two orders of magnitude (about 206 times) greater than the electron mass, the adiabatic approximation is sufficient for understanding μ^+ -electron interaction. In fact, the difference in the Bohr radius between a μ^+ binding a single electron, known as muonium, and the corresponding H^0 atom in vacuum is only 0.43%, implying that they

have nearly the same electronic structure in the matter. Hereafter, the elemental symbol Mu will be introduced to denote μ^+ as pseudo-H, and the valence electronic states of Mu will be denoted as Mu^+ , Mu^0 , and Mu^- . For deliberately avoiding distinction between Mu^+ and Mu^- , both are referred to together as “diamagnetic Mu” and Mu^0 is called “paramagnetic Mu”.

In comparing experimental and theoretical results, there is an important issue to be pointed out at this stage. In conventional μ SR experiments, μ^+ s are implanted as a relatively high-energy ion beam (typical kinetic energy of ~ 4 MeV), which generates free carriers and excitons in insulator crystals due to the associated electronic excitation towards the end of the radiation track [14, 15, 16]. These often propagate rapidly in the crystal, and there is experimental evidence that Mu acts as a capture center to form relaxed-excited states upon interaction with free carriers and/or excitons [17]. Accordingly, these Mu states do not necessarily correspond to the electronic state predicted from the thermodynamic charge conversion level ($E^{+/-}$) obtained by DFT calculations for thermal equilibrium conditions. Moreover, Mu is often observed to be accompanied by fast spin relaxation, which is due to spin/charge exchange interactions with excited carriers and/or excitons. While these phenomena are not observed for H in thermal equilibrium without such carriers, they can be regarded to simulate H in bulk excited states induced by light or electric fields, and Mu is useful as a microscopic probe for such states.

Another well-known evidence that Mu exhibits relaxed-excited states is that two or more different Mu electronic states are often observed simultaneously in the same material. In particular, two paramagnetic Mu states, the tetrahedral center Mu^0 and the bond center Mu^0 , have long been known in elemental semiconductors and III-V compound semiconductors [18], and these have been attributed to the states associated with the temporal acceptor and donor levels ($E^{0/-}$ and $E^{+/0}$) rather than $E^{+/-}$ [19]. With this in mind, we have recently focused on the diamagnetic Mu states, which are observed in pairs with Mu^0 in many wide-gap oxides but whose origin has been unexplored, and conducted an extensive survey to compare the previous experimental results and DFT calculations in the literature. As a result, assuming that the diamagnetic Mu corresponds to the donor-like state which is ionised because the $E^{+/0}$ level is located within the conduction band, we found that the valence of the paired Mu states can be predicted from the positions of $E^{0/-}$ and $E^{+/0}$ in the band structure [17]. This allows us to describe the previous experimental results in a

unified manner, and we call it the ‘‘ambipolarity model’’ because it is ascribed to the fact that the ambipolarity, which is the true nature of H, is expressed through these relaxed-excited states.

MgH₂ crystallises in a stable rutile structure with few H vacancies at ambient condition (the decomposition reaction is endothermic [4]). It is a typical ionic insulator with a band gap above 5 eV, and the ambipolarity model combined with the results of DFT calculations for H predicts that Mu simultaneously takes on both acceptor and donor-like electronic states. The present experimental results are consistent with this prediction, suggesting that the ambipolarity model holds semi-quantitatively in MgH₂. In the following, we will therefore organise the experimental results in terms of this model and attempt to interpret them based on their consistency with the predictions from the corresponding DFT calculations.

2. μ SR Experiment and DFT Calculations

The sample used for μ SR measurements was obtained from a commercial vendor (Fujifilm Wako Chemicals Co.) as a powdered reagent sealed with inert gas. Immediately after opening the container, approximately 2 g of the powder was pressurised and shaped into a disk covered with aluminum foil, mounted on a temperature-controlled cryostat, and then degassed into a vacuum. The μ SR experiments were performed using the ARTEMIS spectrometer installed in the S1 area at the Materials and Life Science Experimental Facility in J-PARC, where a nearly 100% spin-polarised pulsed muon beam (25 Hz, with the full width at half-maximum of 80 ns and a momentum of 27 MeV/c) was transported to the sample. μ SR spectra [time-dependent positron asymmetry, $A(t)$] were measured from room temperature to 5 K in zero magnetic field (ZF) and under longitudinal magnetic fields (LF, 0.01–0.4 T).

The donor/acceptor levels for H assessed in this work are those based on Ref. [13]. They performed DFT calculations with screened hybrid functions of Heyd, Scuseria, and Ernzerhof (HSE) as implemented in the Vienna *Ab initio* Simulation Package (VASP) code. The amount of exact exchange mixed into the HSE generalized gradient functional is taken to 33%, which reproduces the experimentally observed lower limit of the band gap (5.2 eV). Defect calculations were performed for a supercell containing 72 atoms with $2 \times 2 \times 3$ iterations of the primitive cell. A mesh of $2 \times 2 \times 2$ special k points and an energy cutoff value of 270 eV for the plane-wave basis set were used for the defective supercells. For charged defects, the number of electrons in the supercell was varied according to the format described in Ref. [20] and the electrons were localized on the impurity.

We have also performed DFT calculations to investigate in detail the local structure of H-related defects and to evaluate hyperfine parameters of Mu^0 and Δ of the diamag-

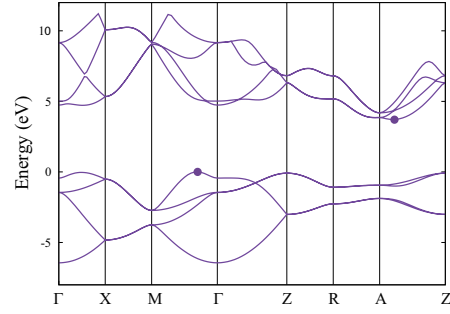


Figure 1. Band structure of MgH₂ calculated by QUANTUM ESPRESSO code (see text). Filled circles indicate the conduction band minimum and valence band maximum.

netic Mu; the comparison of these with experimental values allows us to identify the corresponding donor/acceptor states involving Mu. The DFT calculations were within the generalized gradient approximation (GGA) and the projector augmented wave method as implemented in the QUANTUM ESPRESSO (QE) code [21]. The defects were simulated using 48-atom host supercell with $2 \times 2 \times 2$ iterations of the primitive cell, and the Brillouin-zone integrations implemented by summations over a Monkhorst-Pack k -point mesh of $3 \times 3 \times 5$, with an energy cutoff of 100 Ry for the plane-wave basis set. The calculated lattice parameters $c = 0.301$ nm, $c/a = 0.668$, and $u = 0.304$ are in good agreement with experimental values of 0.301 nm, 0.67, and 0.304 [22]. The band structure calculated for special k -points is shown in Figure 1, which is in good agreement with the previous GGA calculations for the host [12]. It is noteworthy that the band gap is indirect (3.71 eV), and that the relatively steep dispersion near the conduction band minimum (CBM) and valence band maximum (VBM) suggests high mobility of excited carriers as well as a long lifetime.

3. Result

Figure 2 shows the observed ZF/LF- μ SR time spectra at characteristic temperatures. It can be seen that $A(t)$ mainly consists of two components, a paramagnetic component (labeled Mu_p) whose asymmetry is gradually recovered by LF $\simeq 0.05$ –0.4 T and a component described by the Kubo-Toyabe function at ZF [equation (A3)] [23]. At lower temperatures, two more components emerges in the low LF range [Figure 2(a), labeled Mu_{p2} and Mu_{3S} , respectively], suggesting that the spectra consist of four components in total.

It is also noticeable in Figure 2(a) that these four components appear sequentially with increasing LF. This indicates that their hyperfine interactions (including those with nuclear magnetic moments) are mutually distinct, and each component can be identified by the magnitude of its characteristic LF. Therefore, even though these spectra

do not show a significant change with temperature, a reliable analysis can be performed by building a model that reproduces their detailed LF dependence. In fact, it turns out from the LF-dependence that Mu_p and Mu_{p2} components are paramagnetic states, while Mu_{3S} and Mu_{KT} are diamagnetic states. The Mu_{3S} component, which shows relatively fast exponential relaxation, is interpreted to be due to the H-Mu-H complex according to the previous report [24].

A closer look at the time spectra shows that, in order to correctly reproduce their time evolution, it is necessary to take into account the effects of the various spin/charge dynamics to which these states are subjected. More specifically, the sharp decrease of the initial asymmetry $[A(0)]$ in the spectra at 0–10 mT from 0.22 ($=A_{\text{tot}}$) to the value roughly corresponding to that of Mu_{KT} [$A_{KT} \sim 0.09$ –0.14] within $\sim 0.5 \mu\text{s}$ at all temperatures suggests that the asymmetry corresponding to the spin-triplet state of Mu_p [$\simeq (A_{\text{tot}} - A_{KT})/2$, see equation (A10) in Appendix A] is lost due to the fast spin/charge exchange reaction with the excited carriers [18] or some epithermal processes [25, 26, 27]. In Figures 2(a), (d) and (e), there are non-relaxing asymptotic components in the spectra with LF ≥ 50 mT, whose asymmetry recovers with increasing LF, suggesting a transition to the diamagnetic state (labeled Mu_d) via an irreversible charge conversion reaction [28]. Furthermore, in the spectra in Figures 2(b) and (c), the final Mu_d state shows a slow relaxation where the decay rate is almost independent of LF, suggesting that fast fluctuations of the hyperfine field occur with increasing temperature even in the final state.

Based on the above observations, the time spectra were analyzed by the least-squares curve fits using the following phenomenological model for the spin/charge dynamics.

$$A(t) = A_{pd}G_{pd}(t) + A_{p2}G_{p2}(t) + A_{KT}G_z^{KT}(t) + A_{3S}G_z^{3S}(t), \quad (1)$$

$$G_{pd}(t) = fe^{-(\lambda_p + \kappa)t}g_z(x_p) + (1-f)e^{-\lambda_d t}, \quad (2)$$

$$\lambda_p = \frac{v_p}{2(1+x_p^2)}, f = \frac{\lambda_p}{\lambda_p + \kappa}, \lambda_d \simeq \frac{2\Delta_d^2 v_d}{\omega^2 + v_d^2}, \quad (3)$$

$$G_{p2}(t) = e^{-\lambda_{p2}t}g_z(x_{p2}), \lambda_{p2} \simeq \frac{v_{p2}}{2(1+x_{p2}^2)}, \quad (4)$$

where A_{pd} is the sum of partial asymmetry for Mu_p and Mu_d components, A_{p2} , A_{KT} , and A_{3S} are the partial asymmetry of the respective Mu_{p2} , Mu_{KT} , and Mu_{3S} ($A_{\text{tot}} = A_{pd} + A_{p2} + A_{KT} + A_{3S}$), $G_z^{KT}(t; \Delta_{KT}, \nu_{KT})$ is the Kubo-Toyabe function for Mu_{KT} with Δ_{KT} and ν_{KT} being the linewidth and fluctuation frequency, $G_z^{3S}(t; \omega_{3S}, \lambda_{3S})$ is the relaxation function for the H-Mu-H complex state, f is the fractional yield of Mu_p , v_p is the spin/charge exchange rate, κ is the charge conversion reaction rate from Mu_p to Mu_d [28], $g_z(x) = (\frac{1}{2} + x^2)/(1 + x^2)$ is the initial polarization of the paramagnetic Mu, $x_p = B_0(\gamma_\mu - \gamma_e)/\omega_p$, ω_p is the

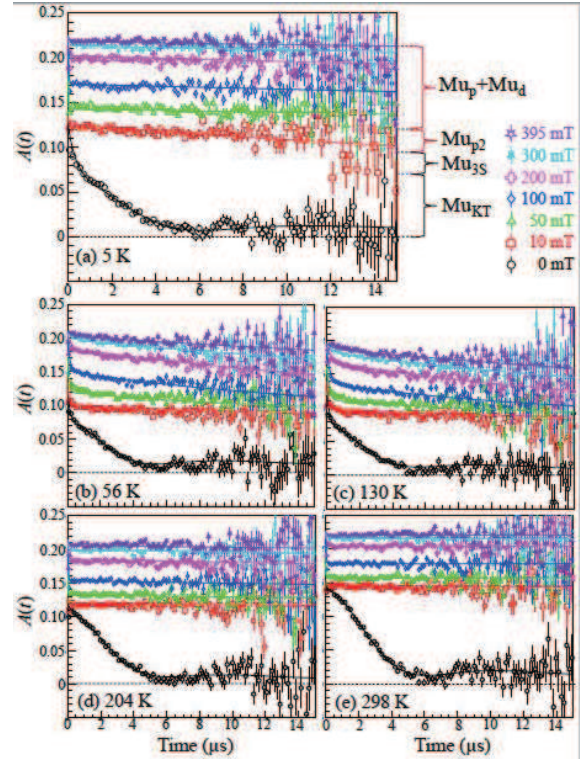


Figure 2. μSR time spectra under zero and longitudinal magnetic fields in MgH_2 at typical temperatures. (a) 5 K, (b) 56 K, (c) 130 K, (d) 204 K, (e) 298 K. (a) Right: time spectrum shows an initial paramagnetic Mu (Mu_p , whose asymmetry is recovered by a longitudinal field) that exhibits conversion to a diamagnetic Mu state (Mu_d). Another paramagnetic state (Mu_{p2} , showing fast relaxation) and a diamagnetic Mu component showing the lineshape well represented by the Kubo-Toyabe relaxation function (Mu_{KT}) can be seen. The solid line shows the result of the global fit based on the model (see text).

hyperfine parameter (angular frequency) of Mu_p , Δ_d is the nuclear magnetic dipolar linewidth, $\omega = \gamma_\mu B_0$, and v_d is the fluctuation rate of Δ_d including the effect of spin/charge exchange reaction. The parameter f is determined by the competition between κ (varies with temperature) and λ_p , and it also depends on LF. For Mu_{p2} , the relaxation due to the spin/charge exchange reaction (λ_{p2}) is considered as in the case of Mu_p . v_{p2} is the spin/charge exchange rate for the Mu_{p2} component, $x_{p2} = B_0(\gamma_\mu - \gamma_e)/\omega_{p2}$, and ω_{p2} is the hyperfine parameter of Mu_{p2} . [See Appendix A for details on these relaxation functions, including the derivation of the equations (3)–(4).] A schematic representation of the relationship between the four states and the meaning of the parameters in the equations (1)–(4) is shown in Figure 3.

In the curve-fit analysis, ω_p showed a considerable temperature dependence [$\omega_p/2\pi$ ranging from 0.52(4) to 1.73(5) GHz] in correlation with v_p and κ [see Figure A1 in Appendix A]. In particular, in the region where $v_p \gtrsim \omega_p/2\pi$ [above ~ 150 K, see Figure 4(c)], ω_p dropped sharply with decreasing accuracy. This is because the effective hyperfine parameter is reduced when the duration for a 1s orbital

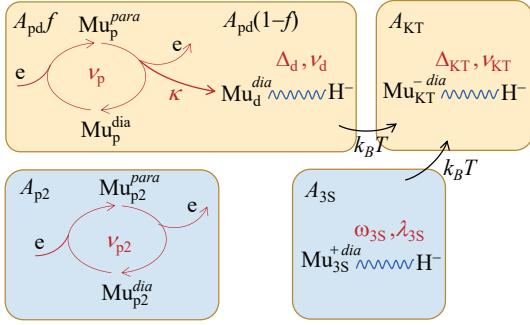


Figure 3. A schematic diagram of the phenomenological model involving Mu_p/Mu_d , Mu_{KT} , Mu_{p2} , and $\text{Mu}_{3\text{S}}$ states and their spin/charge exchange reactions represented by equations (1)–(4). Here, the paramagnetic state are expressed as *para* and the diamagnetic states as *dia*. Since all the initial Mu states are relaxed-excited states (non-equilibrium), the arrow labeled “ kT ” represents the process of approaching thermal equilibrium by annealing as the temperature is increased.

electron to exert a continuous hyperfine field on μ^+ ($\sim 1/v_p$) becomes shorter than the spin rotation period due to the hyperfine interaction ($\sim 2\pi/\omega_p$) [18, 29, 30]. Such an effect, also known as “motional narrowing” in magnetic resonance, could account for the temperature dependence of ω_p correlated with v_p . In the following, in order to examine the temperature variation of other parameters without the effect of ω_p ambiguity, the analysis was performed with $\omega_p/2\pi$ fixed at 0.721 GHz, the average value below 50 K where A_{tot} was also nearly constant.

Although the result still showed a strong correlation between v_p and κ , this can be reasonably understood by assuming that the charge conversion process occurs as part of the spin/charge exchange reaction (Figure 3, top left). The $\text{Mu}_{3\text{S}}$ signal was hard to be discerned from those of other components above ~ 150 K, and $A_{3\text{S}}$ was set to zero for the analysis of data at higher temperatures. Meanwhile, since ω_{p2} showed a tendency of changing with temperature, we assumed that the hyperfine interaction of the second paramagnetic component Mu_{p2} could change with temperature (see below). As indicated by the solid curves in Figure 2, this phenomenological model reasonably reproduces the experimental data including the LF dependence at all temperatures. The temperature dependence of the parameters obtained from the curve-fits is shown in Figure 4.

The electronic state of Mu_p^0 is characterized by a relatively large hyperfine parameter ($\omega_p/\omega_{\text{vac}} \sim 0.12\text{--}0.39$). As is evident in Figures 4(a), (b) and (c), the decrease in A_{pd} and total signal amplitude A_{tot} seen over 50–150 K is in line with the decrease in conversion rate κ . On the other hand, v_p appears to be almost constant over this temperature range. Therefore, the decrease of A_{pd} and A_{tot} suggests that the spin relaxation is induced by the fast spin/charge exchange reaction (v_p) as the lifetime of the Mu_p state (κ^{-1}) becomes longer. The magnitude of Δ_d provides a clue to the

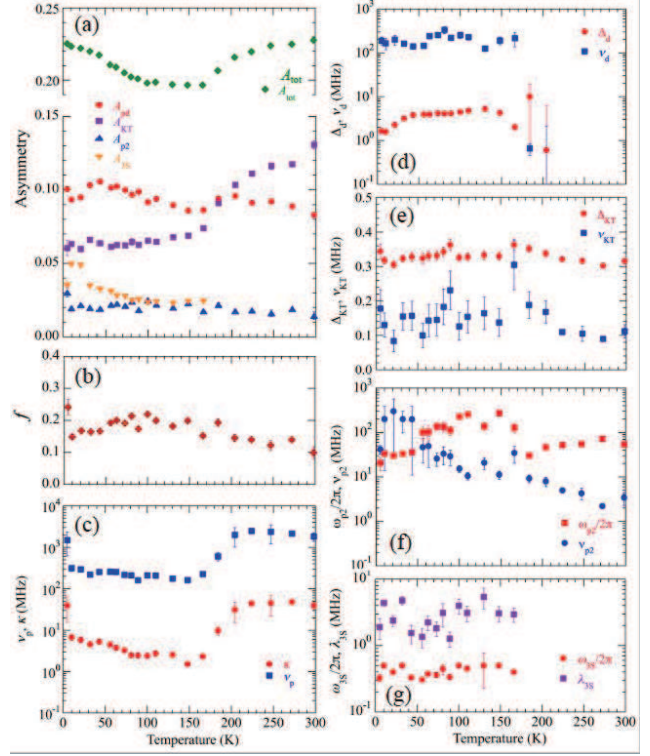


Figure 4. Temperature dependence of the parameters obtained from the analysis of ZF/LF- μ SR time spectra: (a) the initial asymmetry of each component, (b) the fractional yield of Mu_p , (c) spin/charge fluctuation frequency of the Mu_p component (v_p) and conversion rate to Mu_d (κ), (d), (e) nuclear dipolar linewidths of Mu_d and Mu_{KT} (Δ_d and Δ_{KT}) and their fluctuation frequencies (v_d and v_{KT}), (f) hyperfine parameters of the Mu_{p2} component (ω_{p2}) and its spin fluctuation frequency (v_{p2}), (g) the precession frequency ($\omega_{3\text{S}}$) and relaxation rate ($\lambda_{3\text{S}}$) of the H-Mu-H three-spin system.

local electronic structure of the final Mu_d state. As shown in Figure 4(d), the average value of Δ_d in the 50–150 K region is 2.71(2) MHz.

Regarding Mu_{KT} characterized by the quasi-static Kubo-Toyabe relaxation, the magnitude of the linewidth Δ_{KT} again provides a strong clue to the microscopic local structure. As shown in Figure 4(e), Δ_{KT} is 0.30–0.36 MHz in all temperature regions, while it is calculated to be greater than 0.63 MHz for any interstitial site without lattice relaxation. Although an exotic Mu state in which Mu is delocalized over two neighboring sites has been proposed in previous studies [31], another possibility is more likely from DFT calculations for H, as discussed below.

While the accuracy of the deduced parameters shown in Figure 4(f) seems limited due to its small amplitude ($A_{p2}/A_{\text{tot}} \simeq 5\text{--}10\%$), we find for the Mu_{p2} component that the entire time spectrum can be consistently reproduced when we assume that the relaxation is that exhibited by a paramagnetic state with $\omega_{p2}/2\pi = 20(7)\text{--}274(41)$ MHz. The magnitude of ω_{p2} is a few % of ω_{vac} and significantly smaller than ω_p . It is noticeable that ω_{p2} shows an increase

of almost one order of magnitude in the 50–150 K region from both low and high temperatures. As discussed before, the effective hyperfine parameter would be reduced when $\nu_{p2} \gtrsim \omega_{p2}/2\pi$, which seems to be the case for the change below ~ 50 K. On the other hand, the decrease above 150 K is not accompanied by such an increase in ν_{p2} . Therefore, this may suggest a transition to a new paramagnetic state. It should be noted, however, that artifacts from the analysis with fixed ω_p may have affected the results.

Finally, let us give a brief overview on the Mu_{3S} state. The corresponding signal exhibits relatively large relaxation rate at all temperatures, $\lambda_{3S} \gg \omega_{3S}$, which makes it difficult to clearly identify the oscillatory signal characteristic to the three-spin systems. While the mean value of $\omega_{3S}/2\pi$ averaged over temperature can be derived to be 0.41(2) MHz [$\omega_{3S} = 2.6(1)$ MHz, corresponding H-Mu distance $r_t = 0.098(5)$ nm], the actual systematic uncertainty is presumed to be larger than that determined statistically. The signal appears to merge with that of the Kubo-Toyabe component above ~ 150 K, implying the instability of the H-Mu-H state.

4. Discussion

4.1. Predictions based on the ambipolarity model and DFT calculations

In order to compare these results with the predictions of ambipolarity model plus DFT calculations, we extracted information related to the formation energy of H-related defects from the literature [13] and summarized it for Mu as shown in Figure 5. The thermodynamic defect formation energy Ξ^q of H^q (with $q = 0, \pm$ being the valence) in a certain material is evaluated by DFT calculations using the following formula,

$$\Xi^q(E_F) = E_{\text{tot}}[\text{H}^q] - E_{\text{tot}}[\text{host}] + qE_F + n_H\mu_H, \quad (5)$$

where $E_{\text{tot}}[\text{H}^q]$ and $E_{\text{tot}}[\text{host}]$ are the total energies calculated for the supercell with and without H^q between lattices, respectively, and E_F is the Fermi energy. μ_H is the H chemical potential that represents the change in Ξ^q when H is removed ($n_H = -1$) or added ($n_H = +1$) to the host crystal upon defect formation. We assume that Mu's experimental results correspond to calculations in the limit where the added H is dilute, i.e., under H-poor conditions in terms of chemical potential. This is supported by the fact that the sample was immediately transferred from the inert gas-tight container to a vacuum environment, where the H partial pressure in the sample environment was kept negligibly small. In addition, previous μSR experiments have shown that the yield of H-Mu-H complexes, which assumes the pre-existence of extra H_i atoms, is small for as-prepared samples and increases with dehydrogenation processes such as milling and oxidation catalyst incorporation [24]. The present experimental result is similar to that of this as-prepared

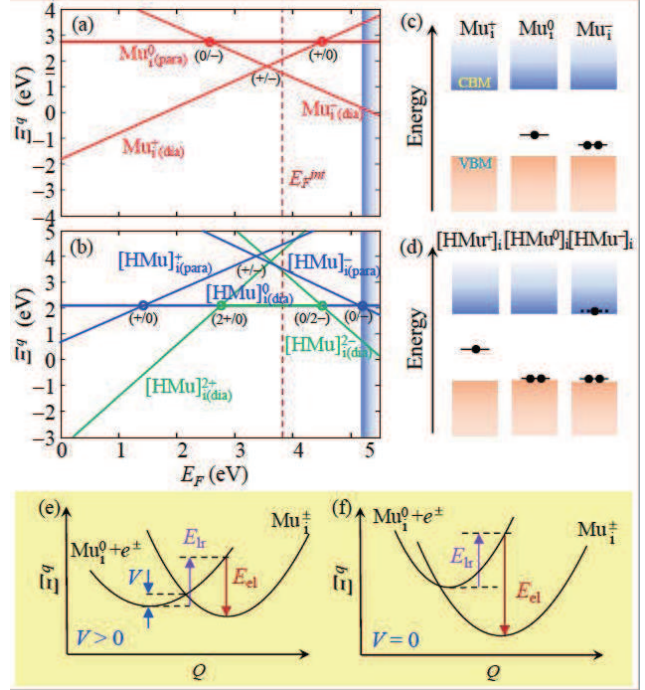


Figure 5. The formation energy (Ξ^q) of H-related defects vs the Fermi level (E_F) in MgH₂ obtained by DFT calculations, where (a) is for the case of interstitial H atoms (H_i^q , $q = 0, \pm$), and (b) is for the interstitial molecules ($[\text{HMu}]_i^q$, $q = 0, \pm, 2\pm$), respectively corresponding to Mu_i and $[\text{HMu}]_i$. The paramagnetic states are expressed as “para” and the diamagnetic states as “dia”. The levels for acceptor ($E^{0/-}$) and donor (E^{+0}) are determined as cross points between $\Xi^\pm(E_F)$ and $\Xi^0(E_F)$. The dashed line shows the intrinsic charge neutral level (E_F^{int}) obtained from the DFT calculation. (Adapted from Ref. [13]) Schematic band diagrams for the single electron energy associated with the donor/acceptor levels (single-charge conversion levels only) in (a) and (b) are shown in (c) and (d), respectively. The level indicated by a dashed line near the CBM in (d) is a shallow state suggested from DFT calculations. For the corresponding local electronic structure, see Figures 6, 7. (e), (f) Schematic of Ξ^q versus configuration coordinate (Q) for $\text{Mu}_i^0 + e^\pm$ and the charged states, where E_{lr} is the lattice relaxation energy, E_{cl} is the Coulomb energy, and V is the potential barrier between the two states. Mu_i^0 is expected to be observed as a relaxed excited state for (e) $V > 0$ but not for (f) $V = 0$.

sample (see below), suggesting that the amount of extra H_i was small. We also point out that a part of the extra H_i contributing to the H-Mu-H complexes could be that ejected from the lattice point by elastic scattering with incident muons (see Appendix B).

Based on Figure 5 and the ambipolarity model, the following predictions can be made. Firstly, regarding the general trend of Ξ^q obtained for interstitial H (H_i) shown in Figure 5(a), the $E^{0/-}$ and E^{+0} levels are on the higher energy side than the $E^{+/-}$ level, indicating the negative U character due to strong electron-phonon interactions [32]. Moreover, both $E^{0/-}$ and E^{+0} form apparently deep in-gap levels, in which the existence of two paramagnetic Mu states (Mu_i^0 's) may be expected. However, as shown in Figures 5(e) and (f), whether Mu_i^0 can actually exist as a relaxed excited state depends on the presence of a potential

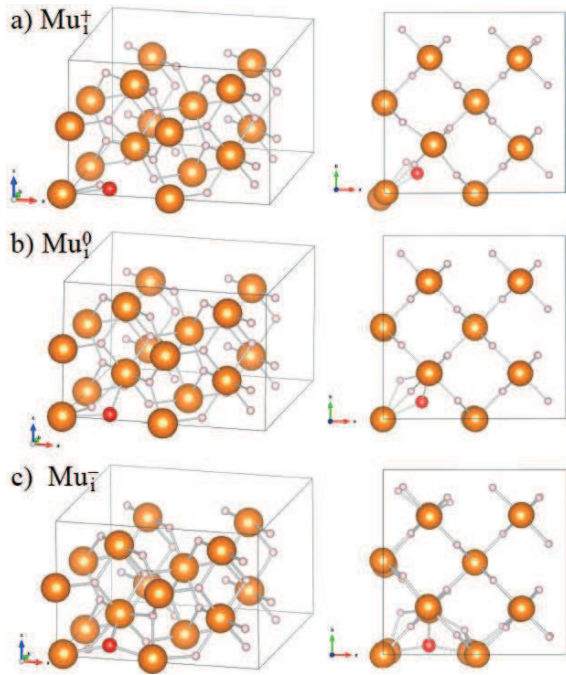


Figure 6. Local structure of interstitial H (H_i) in (a) positive, (b) neutral, and (c) hydride states which are substituted with Mu (red balls), viewed from *b* (left) and *c* (right) axes, respectively.

barrier V at the transition to the charged states. As we will see below, $V > 0$ is inferred for the transition to Mu_i^+ , while $V \simeq 0$ is suggested for the transition to Mu_i^- because the Mu_i^0 state corresponding to the acceptor level is not observed in the experiment (although this does not rule out the possibility of short-lived Mu_i^0). Note that the one-electron energy levels shown in Figure 5(c) correspond to E_{el} , not $E^{-/0}$. Regarding the H_i^- state (corresponding to Mu_i^-), it is predicted to accompany significant local lattice relaxation; H_i^- pushes away the surrounding ligand H^- atoms by 0.052 nm while it attracts Mg^{2+} [12]. On the other hand, the charged donor-like H (H_i^+ , corresponding to Mu_i^+) binds strongly to the ligand H, forming a neutral HMu molecule corresponding to the onsite H_2 molecule [12]. The single-electron energetics are shown in Figure 5(c).

Secondly, provided that Mu can form an interstitial molecule with a pre-existing H_i atom (denoted as $[HMu]_i$), the electronic states for the interstitial H_2 molecules ($[H_2]_i$) predicted by the DFT calculations can provide the basis for discussing those of $[HMu]_i$. As shown in Figure 5(b), the $[HMu]_i^0$ state is stable over a wide E_F region in the band gap, showing lower formation energy than that for $[HMu]_i^+$ and $[HMu]_i^-$ (i.e., positive- U), and can exist even in thermal equilibrium. The $E^{0/-}$ and $E^{+/0}$ levels are closer to the band edge than for the isolated Mu, and $E^{0/-}$ appears to overlap the conduction band minimum (CBM). Regarding the local structure, the $[HMu]_i^+$ molecule is pulled to ligand H^- to form a paramagnetic complex state

(see below). The double charge conversion levels for $[HMu]_i^{2+}$ and $[HMu]_i^{2-}$ are closer to the charge neutral level (E_F^{int}) and form deeper levels. The $[HMu]_i^{2+}$ molecular states are unstable, and both H and Mu are presumed to form onsite neutral H_2 and HMu molecules with ligand H^- , respectively. The corresponding single-electron energetics are shown in Figure 5(d).

4.2. Local electronic structure of each Mu state

In order to obtain further clues about the correspondence between these DFT predictions and the experimental results for Mu, we have investigated the local defect structure associated with these acceptor/donor levels in each of the above two cases by QE calculations. The obtained local structures for H_i and $[H_2]_i$ are shown in Figures 6 and 7, respectively, where those for H_i are in good agreement with earlier GGA results using VASP code [12]. We found that the $E^{+/0}$ level associated with H_i ($= Mu_i$) and that of the $[H_2]_i$ molecule ($= [HMu]_i$) have a finite unpaired electron density in the band gap (i.e., the paramagnetic states). This is consistent with the experimental observation of two paramagnetic states, Mu_p and Mu_{p2} . The hyperfine parameters calculated by GIPAW module of the QE suite for these states are listed in Table 1. They exhibit a common character that the Fermi contact interaction is predominant. For the other diamagnetic states, the nuclear dipolar width Δ are summarized in Table 2.

Given that the Mu states associated with the defect levels in Figure 5(c) and (d) are meaningful only in the non-equilibrium state, there is no guarantee that the electronic structures of Mu discussed below correspond to those in thermal equilibrium. However, since the latter are generally not significantly altered by E_F , it is reasonable to assume that, among the relaxed-excited states, those that can also exist in thermal equilibrium have the same electronic structure as the latter. Specifically, for the Mu_i states (negative- U centers), Mu_i^0 has no corresponding state in thermal equilibrium, but Mu_i^\pm states correspond to those in thermal equilibrium (and to H_i^\pm); for the $[HMu]_i$ molecules (positive- U centers), all states possibly correspond to those in thermal equilibrium (and to $[H_2]_i$). In light of the above considerations, we discuss the correspondence between these levels and the experimentally observed Mu states.

• Mu_p and Mu_d

As mentioned earlier, there is considerable uncertainty in the experimental estimate of ω_p (see the bottom row of Table 1 and Figure A1), making it difficult to determine whether Mu_p corresponds to Mu_i^0 or $[HMu]_i^+$ from the value of ω_p alone. Since Mu_p/Mu_d is considered to be a pair with Mu_{KT} from the ambipolarity model, let us first discuss the attribution of Mu_d . The empirical rule in the model suggests that the yields of paired acceptor-like and donor-like Mu are nearly equal to satisfy overall charge neutrality. Given that A_{pd} is comparable with A_{KT} over

the wide temperature range and that Mu_{KT} is attributed to Mu_i^- (see below), it is reasonable to ascribe Mu_d to Mu_i^+ , and thus Mu_p is ascribed to Mu_i^0 . The latter is also in line with the fact that the maximum value of ω_p [= $2\pi \times 1.73(5)$ GHz, realized when the ‘‘motional narrowing’’ effect is negligible] is about 86% of the value predicted from ω_c of H_i^0 (= $2\pi \times 2.003$ GHz), which is closer than that of $[\text{H}_2]_i^+$ (= $2\pi \times 0.85\text{--}0.86$ GHz). Furthermore, this result indicates that the potential barrier for the transition from Mu_i^0 to Mu_i^+ is positive [$V > 0$, see Figure 5(e)].

For the experimental value of Δ_d , it can be explained when the H-Mu distance is $r = 0.083$ nm, about 11% larger than the p-p distance of 0.078 nm estimated from

Table 1. Calculated hyperfine parameters for the paramagnetic states: H_i^0 [corresponding to Figure 6(b)] and those for each H in $[\text{H}_2]_i^+$ molecule [I and II in Figure 7(b)]. The values for Mu must be multiplied by 3.18. The bottom rows show experimental values for paramagnetic Mu states in comparison with those for candidate paramagnetic states inferred from DFT calculations.

H_i^0	Magnetic dipolar term (MHz)		Principal axis	
	$\omega_{xx}/2\pi$	-0.0295	(0, 0, 1)	
	$\omega_{yy}/2\pi$	-1.8829	(0.5514, -0.8342, 0)	
	$\omega_{zz}/2\pi$	1.9125	(-0.8342, -0.5514, 0)	
	Fermi contact term (MHz)			
$\omega_c/2\pi$	630.013	—		
$[\text{H}_2]_i^+$	I	Magnetic dipolar term (MHz)		Principal axis
		$\omega_{xx}/2\pi$	-19.1146	(0.4991, -0.8665, 0)
		$\omega_{yy}/2\pi$	-19.5940	(0, 0, 1)
		$\omega_{zz}/2\pi$	38.7086	(-0.8665, -0.4991, 0)
		Fermi contact term (MHz)		
	$\omega_c/2\pi$	267.150	—	
	II	Magnetic dipolar term (MHz)		Principal axis
		$\omega_{xx}/2\pi$	-3.1894	(0, 0, 1)
		$\omega_{yy}/2\pi$	-4.7335	(0.3198, -0.9475, 0)
		$\omega_{zz}/2\pi$	1.9125	(-0.9475, -0.3198, 0)
Fermi contact term (MHz)				
$\omega_c/2\pi$	271.750	—		
Mu	Mu_i^0 (ω_c)	$[\text{HMu}]_i^+$ (ω_c)		
h.f. (GHz)	2.003	(I) 0.849 / (II) 0.864		
Exp. (GHz)	Mu_p (ω_p)	Mu_{p2} (ω_{p2})		
	0.52(4)–1.73(5)	0.020(7)–0.274(41)		

Table 2. Calculated nuclear dipolar linewidth Δ for the diamagnetic Mu states. The bottom row shows experimental values for diamagnetic Mu corresponding to each state in the upper row.

Electronic state	Mu_i		$[\text{HMu}]_i$
	Mu_i^+	Mu_i^-	$[\text{HMu}]_i^{0,2\pm}$
Δ (MHz)	3.64	0.3685	3.2–3.9
Exp. (MHz)	Mu_d (Δ_d)	Mu_{KT} (Δ_{KT})	Mu_{3S} (ω_{3S})
	2.71(2)	0.330(4)	2.6(1)

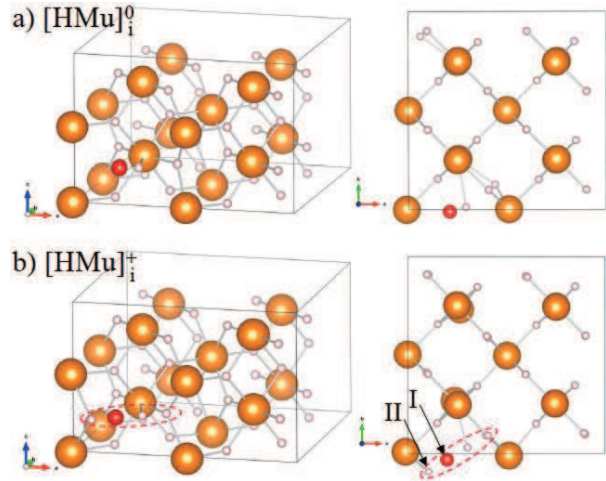


Figure 7. Local structure of an interstitial hydrogen molecule in (a) $[\text{H}_2]_i^0$ and (b) $[\text{H}_2]_i^+$ states with one H atom substituted by Mu (red balls), viewed from *b* (left) and *c* (right) axes, respectively. There are two inequivalent H denoted by labels I and II for (b), where the case with H_1 replaced with Mu is shown. The hyperfine parameters for (b) are distributed over four H atoms indicated by a dashed ellipse.

the QE calculation. The relatively large v_d (150–230 MHz) suggests that even after Mu_p (= Mu_i^0) destabilizes and transitions to Mu_d (= Mu_i^+), a fast spin/charge exchange reaction ($\text{Mu}_i^+ + e^- \rightleftharpoons \text{Mu}_i^0$) persists with the excitonic carriers.

• Mu_{KT}

The linewidth Δ_{KT} of the Mu_{KT} component [= 0.330(4) MHz on average, see Figure 4(e)] is in good agreement with 0.3685 MHz expected for Mu_i^- that accompanies significant outward relaxation of the surrounding H^- . Considering that the incident μ^+ is accompanied by $\sim 10^2$ electron-hole pairs (see Appendix B), it may be allowed to assume that the probability of capturing two electrons and taking the anion state is sufficiently high. As discussed earlier, the reason why the relaxed excited state Mu^0 associated with this state is not observed is presumably because there is no potential barrier for the transition to Mu_i^- [$V \simeq 0$, see Figure 5(f)]. This unusual situation may be related to the large lattice relaxation around Mu_i^- and the strong binding energy due to the associated Coulomb interaction. Thus, Mu_{KT} is ascribed to the diamagnetic state associated with the effective acceptor level of isolated Mu_i (i.e., $\text{Mu}_{\text{KT}}^- = \text{Mu}_i^-$). From the fact that A_{pd} and A_{KT} are comparable and account for the majority of the μSR signal, we conclude that the major part of the observed relaxed-excited Mu states can be explained by the pair Mu_i^+ and Mu_i^- .

• Mu_{p2}

Apart from the cases below 50 K, where $v_{p2} > \omega_{p2}$ and thus ω_{p2} is not well defined, $\omega_{p2}/2\pi$ is 0.1–0.3 GHz for 50–150 K and 20–50 MHz above ~ 150 K, which do not correspond to the hyperfine parameters (ω_c) of any state in Table 1. However, given that Mu_p corresponds to Mu_i^0 , the

only remaining possibility for Mu_{p2} is to be attributed to [HMu]_i⁺.

As shown in Figure 7(b) and Table 1, our QE calculations indicate that the local structure of [H₂]_i⁺ is complicated, resulting in the two inequivalent H sites with different hyperfine parameters (labeled I and II). Since the Fermi contact term may be strongly dependent on the choice of PAW dataset, one cannot rule out the possibility that the calculated value for such a complex local structure may be highly indeterminate. Meanwhile, ω_{p2} is comparable with the value expected from the dipolar terms: e.g., for [H₂]_i⁺-I, the powder average [(ω_{xx}² + ω_{yy}² + ω_{zz}²)/3]^{1/2} × 3.18 = 87.4 MHz. Although this may just be a coincidence, it reminds us that such polaronic states have been reported in some wide-gap oxides (e.g., SrTiO₃ [33], which are supposedly induced by Mu-exciton interaction [17]), and Mu_{p2} may correspond to such a state.

• Mu_{3S}

The ambipolarity model suggests that the Mu_{3S} state (which is paired with Mu_{p2}) corresponds to the diamagnetic [HMu]_i⁰ state associated with the E^{-/0} level near the CBM. As shown in Table 2, the fact that the value of ω_{3S} is comparable with the calculated Δ also supports this conjecture. Although the fast relaxation of the signal makes it difficult to examine the local electronic structure in detail, it is plausible that the Mu_{3S} state consists of the [HMu]_i⁰ molecule bonded to a ligand H⁻ via the hydrogen bonding. It is likely that the H-Mu-H signal reported earlier also stems from the same complex state. As noted in the discussion about the chemical potential of H in equation (5), since extra H_i must exist beforehand for Mu_{3S} to be observed, the amplitude of the signal should be proportional to the amount of such H_i. Therefore, the present experimental result suggests that a relatively small amount of H_i existed in the as-prepared sample.

• Dynamical model

Applying these attributed electronic states of Mu to the phenomenological model, Figure 3 is updated to Figure 8. Based on this, we consider a scenario that explains the rough temperature variation of each state observed in Figure 4. A_{KT} shows a marked increase above 150 K, which is clearly correlated with the increase in the charge transfer reaction rate κ from Mu_i⁰ (= Mu_p) to Mu_i⁺ (= Mu_d). This suggests that the transition from Mu_i⁰ to Mu_i⁻ via Mu_i⁺ is accelerated by the annealing effect with increasing temperature. A similar transition from Mu_{3S} to Mu_{KT}⁻ is suggested to occur in parallel with that for Mu_i⁺. These annealing-induced transitions are explained by the fact that the formation energy Ξ^q(E_F) of Mu_i⁻ is lower than those of Mu_i⁰ around E_F ≈ E^{+/0} and [HMu]_i⁰ around E_F ≈ E^{0/-}, as shown in Figure 5(a) and (b).

The dynamic model we introduced in equations (1)–(4) cannot distinguish whether the fluctuation of the internal magnetic field felt by Mu is due to carrier motion or self-

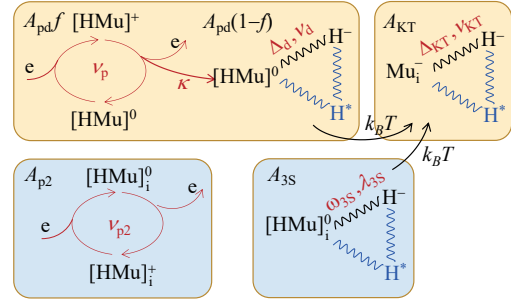


Figure 8. The electronic states of Mu estimated on the basis of the ambipolarity and phenomenological model shown in Figure 3, where Mu_i⁰ = Mu_p, Mu_i⁺ = Mu_d, Mu_i⁻ = Mu_{KT}⁻, [HMu]_i⁺ = Mu_{p2}, and [HMu]_i⁰-H⁻ = Mu_{3S}. The possibility is shown that Mu_i⁺, Mu_i⁻, and [HMu]_i⁰ states may be affected by spin fluctuations of the nearby H centers in the relaxed-excited state (denoted as H*), a factor not explicitly taken into account in the analysis.

diffusion of Mu. The carrier motion is a strong candidate as the cause of the fluctuations, since the band structure in Figure 1 predicts that both electrons and holes are only weakly localized in MgH₂. Regarding the Mu motion, the diamagnetic Mu_i is also considered to be localized (at least in the time scale of μSR) because it is bonded to the ligand H⁻ (Mu_i⁺) or accompanying large lattice distortions (Mu_i⁻, as inferred from ν_{KT}; see the next section for more detail). On the other hand, it is known that the acceptor-like neutral Mu_i⁰ can exhibit rapid long-range diffusion (e.g., in alkali halides [34, 35] and III-V semiconductors [36, 37]). When Mu_i⁰ exhibits self-diffusion, the fluctuation of the nuclear hyperfine (NHF) interaction between 1s orbital electron and proton nuclear spins also induces Mu_i⁰ spin relaxation. In this case, the magnetic field dependence of the longitudinal relaxation rate is expected to be weaker than that for λ_p [see equation (3)], and to vary significantly with the jump frequency of Mu_i⁰ [34, 35, 36, 37]. However, λ_p is so large (> 10¹ MHz) over the wide temperature range (5–298 K) that such a possibility as the origin of longitudinal relaxation seems unlikely. Moreover, the present experimental results suggest that even if the Mu_i⁰ state exists, it is converted to Mu_i⁻ in a short lifetime (~ κ⁻¹). Regarding the [HMu]_i states, they have a mass one order of magnitude larger than Mu, and is considered to be even more localized than the diamagnetic Mu_i. Therefore, the values of the dynamical parameters introduced in the model can be interpreted as mainly reflecting the carrier motion.

Finally, regarding the initial electronic states of Mu_p/Mu_d-Mu_{KT} pair (i.e., Mu_i⁰/Mu_i⁺ and Mu_i⁻), neutral and negative ionic states are predominant as a whole. As shown in Figure 5, the E_F^{int} level is close to the CBM, and the formation energy at E_F^{int} for all electronic states is neutral or negative ionic ground state. Therefore, the population of Mu valence for the relaxed-excited states implies that the overall charge average is close to that of

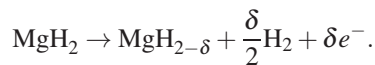
thermal equilibrium. In other words, the reason why Mu (and H) simultaneously assumes donor and acceptor states in the relaxed-excited state is presumably to maintain the global charge neutrality of the system consisting of the host and H.

In conclusion, assuming that the electronic state of Mu implanted into MgH₂ takes the two pairs of defect centers (relaxed-excited states) associated with the donor/acceptor levels for interstitial Mu and HMu molecule states predicted from the DFT calculations, a scenario that coherently describe the present experimental results can be constructed.

4.3. Implications to the kinetics and diffusion of interstitial H

Now, let us discuss what we can learn for H kinetics from these results. It has been reported that the addition of a few % of transition metals such as Ti significantly improves the H kinetics [38, 39, 40]. DFT calculations suggest that, when a transition metal exhibits negative U character to accompany a double charge conversion level $E_{\text{TM}}^{+/-}$ in the host, the addition of the transition metal is expected to shift the Fermi level by $\Delta E = E_{\text{TM}}^{+/-} - E_{\text{F}}^{\text{int}}$ [13]. As can be seen in Figure 5(a), for $\Delta E > 0$ (as predicted for Ti), the interstitial H is stable in the H_i^- state, and this is assumed to be the cause of the kinetic improvement by avoiding binding of H_i to the ligand H^- .

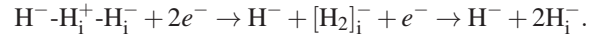
On the other hand, it is also reported that ball milling with a small amount of Nb₂O₅ improves the kinetics [41]. From μSR in the samples after milling with 5 wt% Nb₂O₅, a decrease of the characteristic temperature T_d where diffusion motion of H and/or Mu sets in (as inferred from sharp decrease in Δ_{KT}) from 650 K to about 450 K was observed [24]. Assuming that Nb₂O₅ is an oxidation catalyst and that stabilization of the H_i^- state is the key to improving kinetics, it can be interpreted that Nb₂O₅ raises bulk E_{F} by causing dehydrogenation;



The fact that a similar effect is obtained in the case of ball milling alone suggests that the increased surface area also promotes dehydrogenation reactions by atmospheric oxygen. It is paradoxical that dehydrogenation corresponds to *reduction* for hydrides.

Meanwhile, it has also been reported that the formation of the $\text{Mu}_{3\text{S}}$ state (corresponding to the $\text{H}^- - \text{H}^+ - \text{H}^-$ complex state) is promoted in those samples [24]. Since such hydrogen bond formation is expected to be rather unfavorable from a diffusion point of view, it is assumed that the reason why H kinetics improves with Nb₂O₅ addition is because the effect of stabilizing H_i^- outweighs that of hydrogen bond formation; the upward shift of E_{F}

will eventually lead to the dissociation reaction,



A similar situation is suggested from an earlier μSR study for the effect of Ti-doping to NaAlH₄ [42, 43]

Regarding the Mu_{KT}^- state corresponding to H_i^- , the magnitude of Δ_{KT} is found to vary little over the entire temperature range, indicating that the Mu site remains unchanged over the time range of $\sim 10^1 \mu\text{s}$. The fluctuation frequency ν_{KT} shows nearly constant value of ~ 0.1 MHz below 150 K, which is unlikely to be attributed to thermally activated diffusive motion of Mu_{KT}^- . The non-monotonic temperature dependence of ν_{KT} above 150 K also suggests that the cause is non-thermal. In addition, the paramagnetic Mu components ($\text{Mu}_{\text{p}}/\text{Mu}_{\text{d}}$ and $\text{Mu}_{\text{p}2}$) show fast spin and/or charge exchange reactions with excited carriers even below 150 K. Considering that the frequency of paramagnetic fluctuations ($> 10^2$ MHz) are far from the sensitive range for the diamagnetic Mu, these observations suggest that the fluctuations of Δ_{KT} is induced by the relaxation of proton spins of the nearby H('s) in the relaxed-excited states (denoted as H^*) generated upon muon implantation (see Figure 8).

Note that H^* can be any of the observed four Mu states with H substituting for Mu, which may be appropriately referred to $\text{H}_{\text{p}}/\text{H}_{\text{d}}$, H_{KT} , $\text{H}_{\text{p}2}$, and $\text{H}_{3\text{S}}$. The proton spin relaxation rates λ^* in these states can be evaluated by reducing those for the diamagnetic Mu (inferred from Figure 4) by a factor $R^2 \equiv [\gamma_{\text{p}}/\gamma_{\mu}]^2$ ($= 0.0986$) for the same fluctuation frequency as observed in Mu, e.g., $\lambda^* = R^2 \lambda_{3\text{S}} \simeq 0.2\text{--}0.5$ MHz for the $\text{H}_{3\text{S}}$ state. This implies that further experimental verification will be necessary to determine whether the fluctuations of nuclear dipolar fields exerted by H to the Mg atom binding a negative muon (pseudo-Na atom) observed by negative muon μSR [44] can be solely attributed to H diffusion, because the pseudo-Na atoms can accompany nearby H^* 's due to local electronic excitations which are much stronger than that in positive muon implantation [45].

Acknowledgement

We acknowledge helpful discussions with J. Sugiyama, I. Umegaki, and H. Kageyama. The μSR experiments were conducted under the Inter-University Research Program (Proposal No. 2019MS02) supported by the Institute of Materials Structure Science, High Energy Accelerator Research Organization (KEK), Japan. This work was supported by the MEXT Elements Strategy Initiative to Form Core Research Center for Electron Materials (Grant No. JPMXP0112101001), JSPS KAKENHI (Grant Nos. 19K15033, 17H06153, 20K12484, 21H05102), Core-to-Core Program (JPJSCCA20180006), and JST MIRAI Program (JPMJMI21E9).

Data Availability: The data that supports the findings of this study are available within the article.

APPENDIX A: Details of μ SR data analysis

The spin relaxation of the diamagnetic Mu is governed by a random local fields at the Mu site \mathbf{H}_n from the nuclear magnetic moments, and the magnitude of the relaxation rate is determined by the second moment of \mathbf{H}_n ,

$$\Delta^2 = \gamma_\mu^2 \langle |\mathbf{H}_n|^2 \rangle = \gamma_\mu^2 \sum_n f_n \sum_i \sum_{\alpha, \beta} [\gamma_n (\hat{A}_d^{ni})^{\alpha\beta} \bar{\mathbf{I}}_{ni}]^2, \quad (\text{A1})$$

where $\gamma_\mu = 2\pi \times 135.53$ MHz/T is the gyromagnetic ratio of Mu spin, \mathbf{I}_{ni} is the n th kind of nuclear spin at distance r_{ni} ($n = 1, 2$ for ^1H , ^{25}Mg) on the i th lattice point (with $\gamma_n \bar{\mathbf{I}}_{ni}$ being the effective magnetic moment considering the electric quadrupole interaction for $\mathbf{I}_{ni} \geq 1$), γ_n and f_n are the gyromagnetic ratio and natural abundance (or occupation) of the n th nuclear spin, \hat{A}_d^{ni} is the magnetic dipole tensor

$$(\hat{A}_d^{ni})^{\alpha\beta} = \frac{1}{r_{ni}^3} \left(\frac{3\alpha_{ni}\beta_{ni}}{r_{ni}^2} - \delta_{\alpha\beta} \right) \quad (\alpha, \beta = x, y, z), \quad (\text{A2})$$

representing the hyperfine interaction between Mu and nuclear magnetic moments at $\mathbf{r}_{ni} = (x_{ni}, y_{ni}, z_{ni})$ being the position vector of the nucleus seen from Mu. The sum in equation (A1) takes all x, y, z for β , and x, y for the α components that are effective for longitudinal relaxation when \hat{z} is the LF direction; the z component does not contribute to the relaxation because it gives a magnetic field parallel to the Mu spin.

When the coordination of the nuclear magnetic moment viewed from Mu is isotropic and the number of coordination N is sufficiently large ($N \geq 4$), the time-dependent spin relaxation under zero external field is described by the Gaussian Kubo-Toyabe (GKT) function

$$G_z^{\text{KT}}(t; \Delta) = \frac{1}{3} + \frac{2}{3} (1 - \Delta^2 t^2) e^{-\frac{1}{2} \Delta^2 t^2}. \quad (\text{A3})$$

In the case of fluctuating Δ over time (e.g., due to the self-diffusion of Mu), $G_z^{\text{KT}}(t; \Delta)$ is subject to the modulation and adiabatically approaches exponential decay with increasing fluctuation rate ν , where the detailed lineshape of $G_z^{\text{KT}}(t; B_0, \Delta, \nu)$ as a function of ν and LF ($= B_0$) are found elsewhere [23]. For a small number of nuclei, the time evolution of the Mu spin polarization exhibits considerable deviation from the GKT function. The exact time dependence can be derived from the density matrix of the Mu-nucleus spin system for the $N = 1$ and 2 cases [46, 47, 48] and the latter is introduced to describe H-Mu-H hydrogen bonding state [42, 24]. Assuming a static collinear geometry with μ^+ at the center of the line joining two other nuclear spins ($I = 1/2$), the time evolution of muon polarization as a cubic average is calculated by solving a simple three-spin model to yield [46]

$$G_z^{3\text{S}}(t) = \frac{1}{6} \{ 3 + \cos(\sqrt{3}\omega_{3\text{S}}t) + \alpha_+ \cos(\beta_+ \omega_{3\text{S}}t) \}$$

$$+ \alpha_- \cos(\beta_- \omega_{3\text{S}}t) \} e^{-\lambda_{3\text{S}}t}, \quad (\text{A4})$$

where $\alpha_\pm = 1 \pm 1/\sqrt{3}$, $\beta_\pm = (3 \pm \sqrt{3})/2$, $\omega_{3\text{S}}$ is the dipolar interaction frequency

$$\omega_{3\text{S}} = \gamma_\mu \gamma_1 / r_1^3, \quad (\text{A5})$$

with r_1 being the distance between μ^+ and the proton nucleus, $\gamma_1/2\pi = 42.58$ MHz/T for ^1H , and $\lambda_{3\text{S}}$ is the relaxation rate describing the influence of local fields from outer-shell nuclear magnetic moments [48] and spin/charge exchange interaction.

In the case of fast fluctuation ($\nu > \Delta$), we have an approximated form of the GKT function

$$G_z^{\text{KT}}(t; B_0, \Delta, \nu) \simeq \exp(-\lambda t), \quad (\text{A6})$$

where

$$\lambda \simeq \frac{2\Delta^2 \nu}{\omega^2 + \nu^2}, \quad (\text{A7})$$

and $\omega = \gamma_\mu B_0$. Note that when the fluctuation rate satisfies the condition $\nu \gg \omega$, equation (A7) is least dependent on B_0 .

The magnitude of Δ is sensitive to the size of the nearest-neighbor nuclear magnetic moment $\gamma_n \bar{\mathbf{I}}_{ni}$ and the distance $|\mathbf{r}_{ni}|$ from Mu, and the position occupied by Mu as pseudo-H can be estimated by comparing the experimentally obtained Δ with the calculated value at the candidate sites. We used the DipElec code [49] to calculate Δ for MgH₂.

The μ SR time spectrum shown by the paramagnetic Mu is complicated by the hyperfine interaction between μ^+ and the bound electron. In addition to the limited time resolution of pulsed beam experiments, it is difficult to directly observe the Mu spin precession motion associated with transitions between hyperfine levels due to the dominance of fast spin/charge exchange reactions in MgH₂. Even in such a case, important information can be extracted by examining the response of the time spectrum $G_z(t)$ to the LF in detail.

First, consider Mu⁰ under a magnetic field (B_0) applied parallel the initial Mu polarization ($\parallel z$) without spin fluctuations (static). In this case, we have

$$G_z(t) = \frac{1}{2(1+x^2)} \left[(1+2x^2) + \cos(\omega_c \sqrt{1+x^2}t) \right], \quad (\text{A8})$$

where $x = B_0/B_c$ with $B_c = \hbar\omega_c/(\gamma_\mu - \gamma_e)$ being the effective local field exerted on μ^+ , ω_c is the hyperfine parameter (angular frequency for the isotropic Fermi contact term), and γ_e is the electron gyromagnetic ratio ($= 2\pi \times 28024.2$ MHz/T) [18]. For the zero external field ($x = 0$),

$$G_z(t) = \frac{1}{2} (1 + \cos \omega_c t). \quad (\text{A9})$$

The implication is that a half of the ground state is not an eigenstate of the hyperfine interaction, so the corresponding component exhibits oscillation between the spin-singlet and triplet states with ω_c . In a practical material, ω_c is often

smaller than that in a vacuum ($\omega_{\text{vac}} = 2\pi \times 4463.3$ MHz) due to the effect of dielectric constant, etc., but it is often not visible in ordinary time-resolution measurements (i.e., the second term is zero when time-averaged). Thus, half of the implanted muons effectively lose their polarization upon Mu^0 formation (also called the missing fraction), and only the triplet state [the first term of equation (A8)] becomes observable. The situation is similar for $B_0 > 0$, where the time-averaged polarization at $t = 0$ is

$$G_z(t) \simeq \overline{G}_z(0) = \frac{1 + 2x^2}{2(1 + x^2)} \equiv g_z(x). \quad (\text{A10})$$

As x is normalized by ω_c , the field dependence of $\overline{G}_z(0)$ varies with ω_c . Moreover, Mu^0 in MgH_2 is subjected to the NHF interaction between the bound electron and surrounding H atoms which have proton nuclear spins [18]. This further reduces $\overline{G}_z(0)$ to $1/2 \times 1/3 = 1/6$, reflecting the random orientation of the nuclear spins, and leads to a two-step recovery of $\overline{G}_z(0)$ with respect to x [50]. In any case, the magnitude of ω_c can be determined by comparing the magnetic field dependence of experimentally obtained $\overline{G}_z(0)$ with equation (A10).

The effect of spin fluctuations on Mu^0 under LF can be derived by approximating the spin/charge exchange reaction with excited carriers by a strong collision model. In particular, when the reaction rate ν is lower than ω_c , the time-dependent polarization is given by the following equations [28].

$$G_z(t) \simeq g_z(x) \exp(-\lambda t), \quad (\text{A11})$$

$$\lambda \simeq \frac{\nu}{2(1 + x^2)}. \quad (\text{A12})$$

As mentioned in the main text, we attempted to derive the hyperfine parameter (ω_p) of a paramagnetic state (Mu_p) and other kinetics parameters describing its dynamical properties by using equation (3) [whose magnetic field dependence originates from equations (A10)–(A12)] by a global curve fit that simultaneously analyzes the spectra of different magnetic fields. As a result, ω_p increases significantly from around 20 K to 150 K, and shows a sharp decrease at the high temperature side above 150 K [Figure A1(a)]. Moreover, the latter is strongly correlated with the increase of the spin/charge fluctuation rate ν_p , leaving it hardly determined above ~ 150 K [Figure A1(b)]. Therefore, we adopted the hypothesis that the original ω_p should be approximately constant, and derived the temperature dependence of the other parameters with ω_p fixed to some appropriate value. The temperature dependence of ω_p (ω_{p2}) and its relationship to ν_p (ν_{p2}) are discussed in the main text.

APPENDIX B: Muon irradiation effect

In general, the energy imparted in a solid by the irradiation of charged particles consists of two types of energy: the

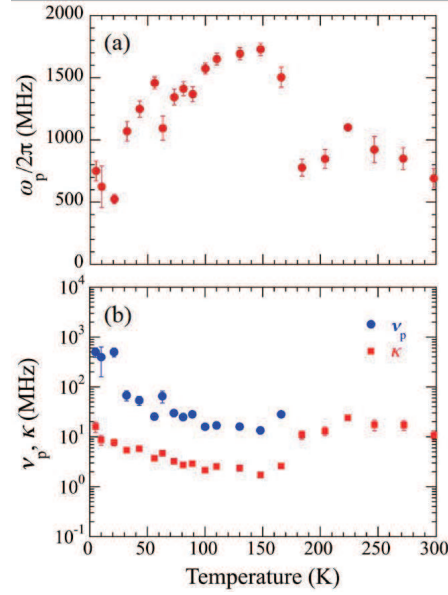


Figure A1. Temperature dependence of (a) the hyperfine parameter (ω_p), (b) spin/charge exchange rate (ν_p) and conversion rate (κ) for the Mu_p state obtained in the first-round analysis in which ω_p was allowed to vary as a free parameter, where ν_p was hardly determined above ~ 150 K.

kinetic energy of the atoms that make up the solid and the excitation energy of the electron system. The former is due to elastic collisions between incident particles and atoms, and the latter is due to inelastic collisions. Irradiation damage (atomic displacement), usually seen in metals and semiconductors, occurs when atoms gain energy above the knock-on threshold ($E_d \simeq 15\text{--}30$ eV) and are ejected from a lattice point [14]. Provided that the mass of the incident particle is m , the energy is E , and the mass of the target atom is M , ejection occurs when the energy ΔE imparted to the atom by the collision exceeds E_d , i.e.,

$$\Delta E = \frac{4mME}{(m+M)^2} > E_d. \quad (\text{B1})$$

When the incident particle is a muon ($m = m_\mu \ll M$), the minimum kinetic energy E_0 required to eject the target atom is given by

$$E_0 = \frac{(m+M)^2}{4mM} E_d \simeq \frac{M}{4m_\mu} E_d. \quad (\text{B2})$$

Therefore, it is inferred that in the region $E > E_0$, muon kinetic energy is consumed mainly by the atomic displacement process.

On the other hand, in the region of $E \leq E_0$ (i.e., $\Delta E \leq E_d$), the energy loss due to excitation of the electronic system becomes dominant. Since the energy required for the formation of electron-hole pairs is known to be approximately $\varepsilon \simeq 2.8E_g$ with the band gap as E_g [15], the number of electron-hole pairs produced is roughly estimated as

$$n_{eh} \simeq \frac{E_0}{\varepsilon} = \frac{E_0}{2.8E_g}. \quad (\text{B3})$$

Assuming $E_d = 30$ eV and $E_g = 5$ eV, the values of E_0 and n_{eh} estimated for the constituent atoms of MgH₂ are summarized in Table B1. From the weighted average of these values, it is estimated that about 10^2 electron-hole pairs per muon are formed in MgH₂. Since such electronic excitations are dominant in the final stage of energy loss of the incident particles, electron-hole pairs are also expected to be distributed near the end of the radiation track.

From the above discussion, H is special in that muons with relatively low kinetic energy are inferred to displace H atoms in solids. Considering that the formation energy of H vacancies in MgH₂ is predicted to be comparable with that for the interstitial H (H_i) [12], it is possible that the ejected H exists as H_i in the vicinity of the muon stopping position.

Table B1. The minimum kinetic energy E_0 of the incident muon required for each target atom to undergo displacement in MgH₂, and the number of electron-hole pairs n_{eh} produced by electronic excitation below E_0 , where $E_d = 30$ eV and $E_g = 5$ eV.

Atom	E_0 (eV)	n_{eh}
H	67	4.8
Mg	1619	116

References

- [1] Dresselhaus M S and Thomas I L 2001 *Nature* **414** 332–337
- [2] Schlapbach L and Züttel A 2001 *Nature* **414** 353–358
- [3] Sakintuna B, Lamari-Darkrim F and Hirscher M 2007 *Int. J. Hydrogen Energy* **32** 1121–1140
- [4] Felderhoff M and Bogdanović B 2009 *Int. J. Mol. Sci.* **10** 325–344
- [5] Huot J, Liang G, Boily S, Van Neste A and Schulz R 1999 *J. Alloys Compd.* **293-295** 495–500
- [6] Oelerich W, Klassen T and Bormann R 2001 *Adv. Eng. Mater.* **3** 487–490
- [7] Fernández J and Sánchez C 2002 *J. Alloys Compd.* **340** 189–198
- [8] Liang G 2004 *J. Alloys Compd.* **370** 123–128
- [9] Conradi M S, Mendenhall M P, Ivancic T M, Carl E A, Browning C D, Notten P H L, Kalisvaart W P, Magusin P C M M, Bowman R C, Hwang S J and Adolphi N L 2007 *J. Alloys Compd.* **446-447** 499–503
- [10] Du A J, Smith S C, Yao X D, Sun C H, Li L and Lu G Q 2008 *Appl. Phys. Lett.* **92** 163106
- [11] Evard E, Gabis I and Yartys V 2010 *Int. J. Hydrogen Energy* **35** 9060–9069
- [12] Park M S, Janotti A and Van de Walle C G 2009 *Phys. Rev. B* **80**(6) 064102
- [13] Roy A, Janotti A and Van de Walle C G 2013 *Appl. Phys. Lett.* **102** 033902
- [14] Thompson M W 1974 *Defects and Radiation Damage in Metals* Cambridge Monographs on Physics (Cambridge University Press, Cambridge)
- [15] Alig R C and Bloom S 1975 *Phys. Rev. Lett.* **35**(22) 1522–1525
- [16] Itoh N 1997 *Nucl. Instr. Meth. Phys. Res. B* **122** 405–409
- [17] Hiraishi M, Okabe H, Koda A, Kadono R and Hosono H 2022 *J. Appl. Phys.* **132** 105701
- [18] Patterson B D 1988 *Rev. Mod. Phys.* **60**(1) 69–159
- [19] Lichti R L, Chow K H and Cox S F J 2008 *Phys. Rev. Lett.* **101**(13) 136403
- [20] Van de Walle C G and Neugebauer J 2004 *J. Appl. Phys.* **95** 3851–3879
- [21] Giannozzi P, Baroni S, Bonini N, Calandra M, Car R, Cavazzoni C, Ceresoli D, Chiarotti G L, Cococcioni M, Dabo I, Corso A D, de Gironcoli S, Fabris S, Fratesi G, Gebauer R, Gerstmann U, Gougoussis C, Kokalj A, Lazzeri M, Martin-Samos L, Marzari N, Mauri F, Mazzarello R, Paolini S, Pasquarello A, Paulatto L, Sbraccia C, Scandolo S, Sclauzero G, Seitsonen A P, Smogunov A, Umari P and Wentzcovitch R M 2009 *J. Phys.: Condens. Matter* **21** 395502
- [22] Bortz M, Bertheville B, Böttger G and Yvon K 1999 *J. Alloys Compd.* **287** L4–L6
- [23] Hayano R S, Uemura Y J, Imazato J, Nishida N, Yamazaki T and Kubo R 1979 *Phys. Rev. B* **20**(3) 850–859
- [24] Umegaki I, Nozaki H, Harada M, Higuchi Y, Noritake T, Matsumoto M, i Towata S, Ansaldo E J, Brewer J H, Koda A, Miyake Y and Sugiyama J 2014 *J. Phys.: Conf. Series* **551** 012036
- [25] Walker D C 1983 *Muon and Muonium Chemistry* (Cambridge University Press, Cambridge)
- [26] Percival P W, Adamson-Sharp K M, Brodovitch J C, Leung S K and Newman K E 1985 *Chemical Physics* **95** 321–330
- [27] Storchak V, Brewer J H, Morris G D, Arseneau D J and Senba M 1999 *Phys. Rev. B* **59**(16) 10559–10572
- [28] Kadono R, Macrae R M and Nagamine K 2003 *Phys. Rev. B* **68**(24) 245204
- [29] Nosov V and Yakovleva I 1965 *Nuclear Physics* **68** 609–631
- [30] Chow K H, Kiefl R F, Hitti B, Estle T L and Lichti R L 2000 *Phys. Rev. Lett.* **84**(10) 2251–2254
- [31] Sugiyama J, Umegaki I, Matsumoto M, Miwa K, Nozaki H, Higuchi Y, Noritake T, Forslund O K, Månsson M, Cottrell S P, Koda A, Ansaldo E J and Brewer J H 2019 *Sustainable Energy Fuels* **3**(4) 956–964
- [32] Anderson P W 1975 *Phys. Rev. Lett.* **34**(15) 953–955
- [33] Ito T U, Higemoto W, Koda A and Shimomura K 2019 *Appl. Phys. Lett.* **115** 192103
- [34] Kiefl R F, Kadono R, Brewer J H, Luke G M, Yen H K, Celio M and Ansaldo E J 1989 *Phys. Rev. Lett.* **62**(7) 792–795
- [35] Kadono R, Kiefl R F, Ansaldo E J, Brewer J H, Celio M, Kreitzman S R and Luke G M 1990 *Phys. Rev. Lett.* **64**(6) 665–668
- [36] Kadono R, Kiefl R F, Brewer J H, Luke G M, Pfiz T, Riseman T M and Sternlieb B J 1991 *Hyperfine Interact.* **64** 635–640
- [37] Kadono R, Matsushita A, Nagamine K, Nishiyama K, Chow K H, Kiefl R F, MacFarlane A, Schumann D, Fujii S and Tanigawa S 1994 *Phys. Rev. B* **50**(3) 1999–2002
- [38] Liang G, Huot J, Boily S, Van Neste A and Schulz R 1999 *J. Alloys Compd.* **292** 247–252
- [39] Varin R A, Czujko T, Wasmund E B and Wronski Z S 2007 *J. Alloys Compd.* **432** 217–231
- [40] Amama P B, Grant J T, Spowart J E, Shamberger P J, Voevodin A A and Fisher T S 2011 *J. Mater. Res.* **26** 2725–2734
- [41] Hanada N, Ichikawa T and Fujii H 2007 *J. Alloys Compd.* **446-447** 67–71
- [42] Kadono R, Shimomura K, Satoh K H, Takeshita S, Koda A, Nishiyama K, Akiba E, Ayabe R M, Kuba M and Jensen C M 2008 *Phys. Rev. Lett.* **100**(2) 026401
- [43] Hiraishi M, Okabe H, Koda A, Kadono R and Hosono H *arXiv:2110.09024*
- [44] Sugiyama J, Umegaki I, Nozaki H, Higemoto W, Hamada K, Takeshita S, Koda A, Shimomura K, Ninomiya K and Kubo M K 2018 *Phys. Rev. Lett.* **121**(8) 087202
- [45] Okumura T, Azuma T, Bennett D A, Caradonna P, Chiu I, Doriese W B, Durkin M S, Fowler J W, Gard J D, Hashimoto T, Hayakawa R, Hilton G C, Ichinohe Y, Indelicato P, Isobe T, Kanda S, Kato D, Katsuragawa M, Kawamura N, Kino Y, Kubo M K, Mine K, Miyake Y, Morgan K M, Ninomiya K, Noda H, O’Neil G C, Okada S, Okutsu K, Osawa T, Paul N, Reintsema C D, Schmidt D R, Shimomura K, Strasser P, Suda H, Swetz D S, Takahashi T, Takeda S, Takeshita S, Tampo M, Tatsuno H, Tong X M, Ueno Y, Ullom J N, Watanabe S and Yamada S 2021 *Phys. Rev. Lett.* **127**(5) 053001

- [46] Brewer J H, Kreitzman S R, Noakes D R, Ansaldo E J, Harshman D R and Keitel R 1986 *Phys. Rev. B* **33**(11) 7813–7816
- [47] Nishiyama K, Nishiyama S W and Higemoto W 2003 *Physica B: Condens. Matter* **326** 41–45
- [48] Wilkinson J M and Blundell S J 2020 *Phys. Rev. Lett.* **125**(8) 087201
- [49] Kojima K M, Yamanobe J, Eisaki H, Uchida S, Fudamoto Y, Gat I M, Larkin M I, Savici A, Uemura Y J, Kyriakou P P, Rovers M T and Luke G M 2004 *Phys. Rev. B* **70**(9) 094402
- [50] Beck R, Meier P F and Schenck A 1975 *Z. Physik B* **22** 109–115